

Projection and Galaxy Clustering Fourier Spectra

J. N. Fry & David Thomas

Department of Physics, University of Florida, Gainesville, FL 32611-8440

ABSTRACT

Second order perturbation theory predicts a specific dependence of the bispectrum, or three-point correlation function in the Fourier transform domain, on the shape of the configuration of its three wave vector arguments, which can be taken as a signature of structure formed by gravitational instability. Comparing this known dependence on configuration shape with the weak shape dependence of the galaxy bispectrum has been suggested as an indication of bias in the galaxy distribution. However, to interpret results obtained from projected catalogs, we must first understand the effects of projection on this shape dependence.

We present expressions for the projected power spectrum and bispectrum in both Cartesian and spherical geometries, and we examine the effects of projection on the predicted bispectrum with particular attention to the dependence on configuration shape. Except for an overall numerical factor, for Cartesian projection with characteristic depth D^* there is little effect on the shape dependence of the bispectrum for wavelengths small compared to D^* or projected wavenumbers $qD^* \gg 1$. For angular projection, a scaling law is found for spherical harmonic index $\ell \gg 1$, but there is always a mixing of scales over the range of the selection function. For large ℓ it is sufficient to examine a small portion of the sky.

Subject headings: large-scale structure of universe

1. Introduction

The behavior of cosmological density fluctuations in perturbation theory is becoming a mature, well-understood subject, allowing analytic calculations of the expected behavior of correlation functions to high order (Fry 1984; Goroff et al. 1986; Bernardeau 1992; Jain & Bertschinger 1994; Scoccimarro & Frieman 1996a,b; Scoccimarro et al. 1998). Starting with Gaussian initial conditions at early times, the first nonvanishing contribution to the n -point correlation function ξ_n requires knowledge of perturbations to order $n-1$. To leading order irreducible point or windowed moments of density follow the hierarchical pattern,

$$\xi_n = \langle \delta^n \rangle_c = S_n \xi_2^{n-1}, \quad (1)$$

first found in observations, where the full galaxy three-point correlation function ζ can be written as a sum of products of two-point functions ξ as (Groth & Peebles 1977)

$$\zeta_{123} = Q_{123} (\xi_{12}\xi_{13} + \xi_{12}\xi_{23} + \xi_{13}\xi_{23}). \quad (2)$$

In observations, of both the three-point function in space and the bispectrum in the Fourier transform domain (Fry & Seldner 1982), the dimensionless amplitude Q depends only weakly on overall scale or on configuration shape. In perturbation theory, the reduced three-point function amplitude, or the corresponding bispectrum amplitude in Fourier space (see eq. [16] below), is not a constant but a function of the lengths of the triangle

or of the three wave vectors that make up the configuration (Fry 1984; Bouchet et al. 1995), a function that varies with the power spectrum index n but depends only weakly on cosmological parameters such as the fraction of critical density Ω_0 and the cosmological constant Λ (Bouchet et al. 1992; Bouchet et al. 1995; Scoccimarro et al. 1998). The apparent disagreement between theory and observation can be understood as an effect of bias. A nonlinear but local bias in the galaxy distribution, with fractional contrast in the galaxy number density determined as a function of the local mass density contrast, $\delta_g = \sum b_k \delta^k / k! \approx b\delta + \frac{1}{2}b_2\delta^2$, gives a galaxy three-point amplitude that depends on the first two coefficients in the expansion (Fry & Gaztañaga 1993),

$$Q_g = \frac{1}{b} Q_{123} + \frac{b_2}{b^2}, \quad (3)$$

where $b = b_1$ is the usual linear bias factor. Matarrese, Verde, & Heavens (1997) have estimated the expected uncertainties and analyzed numerical simulations to investigate the practicality of applying the method to data, and have concluded that the method works well in the unbiased case, with likelihood centered around $b = 1$ and $b_2 = 0$. The local bias model may be an oversimplification, but represents the minimal nonlinear degree of freedom in any nonlinear galaxy formation model. Comparison of the observed galaxy three-point amplitude in the Lick catalog with that expected in perturbation theory using equation (3) provides an estimate for b that is larger than expected from other methods (Fry 1994).

Any measurements that provide information about bias are important for our ability to infer properties of the cosmological mass distribution from galaxy observations. However, many of the largest galaxy compilations, including the Lick catalog, are angular positions only, and an important question is whether angular projection has a significant effect on the results. For angular correlation functions and moments this has been studied for some time (Limber 1953; Rubin 1954; Groth & Peebles 1977; Kaiser 1992; Pollo 1997; Gaztañaga & Bernardeau 1998). In this paper we compute the effects of projection in the transform domain, on the power spectrum and bispectrum. In the following, in Section 2 we first compute a simple Cartesian projection, where we can easily observe the approach to the asymptotic small and large scale results, and present numerical results in Section 3. Following this, we examine angular projection in Section 4, over the full sky and also over a small patch. Section 5 contains a final discussion.

2. Cartesian Projection

For simplicity, we first present results for projection along a Cartesian direction, denoted z . Cartesian projection misses an important scale mixing found below in projection at fixed angular positions, but it is simpler both to compute and to understand, and thus provides a useful guide in understanding later results. The projected number density of galaxies n_p is the space density $n(x, y, z)$, summed over z , weighted by a selection function $F(z)$ that gives the probability that an object at z is included,

$$n_p(x, y) = \int dz F(z) n(x, y, z). \quad (4)$$

For convenience, although this is not necessary we take F to scale with a typical depth D^* , $F = F(z/D^*)$ (Peebles 1980). In an attempt to separate projected and unprojected quantities, in what follows we will write projected functions with a subscript p : n_p , ξ_p , etc. To distinguish positions in the two-dimensional projected space from those in the full three dimensions, we will denote the former as \mathbf{x} and the latter as \mathbf{r} ; similarly, wave vectors in the two-dimensional space we will denote \mathbf{q} and in three dimensions as \mathbf{k} . It will occasionally be necessary to refer to a three-vector made from a two-vector and a third component; $\mathbf{r} = (\mathbf{x}, z)$, $\mathbf{k} = (\mathbf{q}, k)$, etc.; $\mathbf{k} = \mathbf{q}$ means $\mathbf{k} = (\mathbf{q}, 0)$. Thus, equation (4) can equivalently be written $n_p(\mathbf{x}) = \int dz F(z) n(\mathbf{r})$.

We wish to study statistics of the projected density. In space, we write $\langle n(\mathbf{r}) \rangle = \bar{n}$, and the two-point correlation function ξ and the three-point function ζ are defined by

$$\langle n(\mathbf{r}_1)n(\mathbf{r}_2) \rangle = \bar{n}^2 [1 + \xi(\mathbf{r}_{12})] \quad (5)$$

and

$$\langle n(\mathbf{r}_1)n(\mathbf{r}_2)n(\mathbf{r}_3) \rangle = \bar{n}^3 [1 + \xi(\mathbf{r}_{12}) + \xi(\mathbf{r}_{23}) + \xi(\mathbf{r}_{31}) + \zeta(\mathbf{r}_1, \mathbf{r}_2, \mathbf{r}_3)], \quad (6)$$

where angle brackets $\langle \dots \rangle$ indicates an ensemble average, equivalent by homogeneity to an average over space, and \mathbf{r}_{12} is shorthand for $\mathbf{r}_1 - \mathbf{r}_2$. Cosmological symmetries imply that ξ and ζ depend only on distances between points.

Similar expressions hold for projected functions. The average projected density is $\bar{n}_p = \int dz F(z) \bar{n}$, while from equation (4) we can express moments of n_p as integrals over the spatial correlation functions,

$$\bar{n}_p^2 \xi_p(\mathbf{x}_{12}) = \bar{n}^2 \int dz_1 dz_2 F(z_1) F(z_2) \xi(|\mathbf{r}_{12}|), \quad (7)$$

$$\bar{n}_p^3 \zeta_p(\mathbf{x}_1, \mathbf{x}_2, \mathbf{x}_3) = \bar{n}^3 \int dz_1 dz_2 dz_3 F(z_1) F(z_2) F(z_3) \zeta(\mathbf{r}_1, \mathbf{r}_2, \mathbf{r}_3). \quad (8)$$

These are equivalent to relations for projected angular functions (Limber 1953; Peebles 1980).

Because correlations depend only on separations, it is natural to change variables from z_1, z_2 to the appropriate mean $z = \frac{1}{2}(z_1 + z_2)$ or $z = \frac{1}{3}(z_1 + z_2 + z_3)$ and differences $z_{12} = z_1 - z_2$. In the approximation that correlations are small except for small separations, we can write

$$\xi_p(\mathbf{x}_{12}) = \frac{\int dz F^2(z)}{[\int dz F(z)]^2} \int dz_{12} \xi(|\mathbf{r}_{12}|) \quad (9)$$

$$\zeta_p(\mathbf{x}_{12}, \mathbf{x}_{13}) = \frac{\int dz F^3(z)}{[\int dz F(z)]^3} \int dz_{12} dz_{13} \zeta(\mathbf{r}_{12}, \mathbf{r}_{13}) \quad (10)$$

From these, it is apparent that if the spatial three-point function is hierarchical with constant Q (eq. [2]), then so is the projected three-point function, with

$$\frac{Q_p}{Q} = \frac{[\int dz F^3(z)][\int dz F(z)]}{[\int dz F^2(z)]^2}. \quad (11)$$

This result is independent of the normalization of F . By the Schwarz inequality, $Q_p/Q \geq 1$. The equivalent result was obtained in the angular case by Fry & Seldner (1982).

Our goal now is to compute projected moments in the Fourier domain. In Fourier transform space we have the amplitude

$$\tilde{n}(\mathbf{k}) = \int d^3r n(\mathbf{r}) e^{-i\mathbf{k}\cdot\mathbf{r}}, \quad (12)$$

$$n(\mathbf{r}) = \int \frac{d^3k}{(2\pi)^3} \tilde{n}(\mathbf{k}) e^{i\mathbf{k}\cdot\mathbf{r}}. \quad (13)$$

The mean density contributes $(2\pi)^3 \delta_D(\mathbf{k}) \bar{n}$ to $\tilde{n}(\mathbf{k})$. Moments of the Fourier amplitude for $\mathbf{k} \neq 0$ give the power spectrum $P(k)$ and the bispectrum $B(\mathbf{k}_1, \mathbf{k}_2, \mathbf{k}_3)$ (the Fourier transforms of ξ and ζ respectively),

$$\langle \tilde{n}(\mathbf{k}_1) \tilde{n}(\mathbf{k}_2) \rangle = \bar{n}^2 [(2\pi)^3 \delta_D(\mathbf{k}_1 + \mathbf{k}_2)] P(k), \quad (14)$$

$$\langle \tilde{n}(\mathbf{k}_1)\tilde{n}(\mathbf{k}_2)\tilde{n}(\mathbf{k}_3) \rangle = \bar{n}^3[(2\pi)^3\delta_D(\mathbf{k}_1 + \mathbf{k}_2 + \mathbf{k}_3)] B(\mathbf{k}_1, \mathbf{k}_2, \mathbf{k}_3). \quad (15)$$

The “momentum conserving” Dirac δ -function, arising from homogeneity, ensures that the bispectrum is defined only for configurations of wave vectors that form a closed triangle, $\sum \mathbf{k}_i = 0$. The reduced three-point amplitude is defined to be

$$Q(\mathbf{k}_1, \mathbf{k}_2, \mathbf{k}_3) = \frac{B(\mathbf{k}_1, \mathbf{k}_2, \mathbf{k}_3)}{P(k_1)P(k_2) + P(k_1)P(k_3) + P(k_2)P(k_3)} \quad (16)$$

The projected Fourier amplitude is

$$\begin{aligned} \tilde{n}_p(\mathbf{q}) &= \int d^2x n_p(\mathbf{x})e^{-i\mathbf{q}\cdot\mathbf{x}} = \int d^2x dz F(z) n(\mathbf{r})e^{-i\mathbf{q}\cdot\mathbf{x}} \\ &= \int d^3r F(z) \int \frac{d^3k_z}{(2\pi)^3} \tilde{n}(\mathbf{k}_z) e^{i\mathbf{k}_z\cdot\mathbf{r}} e^{-i\mathbf{q}\cdot\mathbf{x}} = \int \frac{dk_z}{2\pi} \tilde{F}^*(k_z) \tilde{n}(\mathbf{q}, k_z), \end{aligned} \quad (17)$$

the spatial amplitude evaluated at $\mathbf{k} = \mathbf{q}$ smeared in the projection direction over $\tilde{F}(k_z) = \int dz F(z)e^{ik_z z}$. Note that if F has typical scale D^* , then \tilde{F} has extent $1/D^*$.

Moments of the projected amplitudes then give the corresponding projected spectra. Normalized by \bar{n}_p these are

$$P_p(q) = \frac{1}{[\int dz F(z)]^2} \int \frac{dk_z}{2\pi} |\tilde{F}(k_z)|^2 P[(q^2 + k_z^2)^{1/2}] \quad (18)$$

$$B_p(\mathbf{q}_1, \mathbf{q}_2, \mathbf{q}_3) = \frac{1}{[\int dz F(z)]^3} \int \frac{dk_{z1}}{2\pi} \frac{dk_{z2}}{2\pi} \tilde{F}(k_{z1}) \tilde{F}(k_{z2}) \tilde{F}(-k_{z1} - k_{z2}) B(\mathbf{q}_1, k_{z1}; \mathbf{q}_2, k_{z2}; \mathbf{q}_3, k_{z3}). \quad (19)$$

These are the basic results of this section.

The large- and small- qD^* limits of these expressions are both of interest. Analogous to the small separation approximation in coordinate space, when D^* is large, \tilde{F} is nonvanishing only for small k_z ; the arguments of P and B are then the transverse \mathbf{q} and can be taken outside the integrals. In this limit the projected spectra are, up to a constant factor, the corresponding spatial function evaluated in the transverse plane, $\mathbf{k} \approx (\mathbf{q}, 0)$. By Parseval’s theorem and a simple generalization, the integrals over k_z can be written as the same integrals over z that appear in equations (9) and (10),

$$P_p(q) \rightarrow P(q) \frac{\int dz F^2(z)}{[\int dz F(z)]^2}, \quad (20)$$

$$B_p(\mathbf{q}_1, \mathbf{q}_2, \mathbf{q}_3) \rightarrow B(\mathbf{q}_1, \mathbf{q}_2, \mathbf{q}_3) \frac{\int dz F^3(z)}{[\int dz F(z)]^3}, \quad (21)$$

$$Q_p(\mathbf{q}_1, \mathbf{q}_2, \mathbf{q}_3) \rightarrow Q(\mathbf{q}_1, \mathbf{q}_2, \mathbf{q}_3) \frac{[\int dz F^3(z)][\int dz F(z)]}{[\int dz F^2(z)]^2} \quad (22)$$

($qD^* \gg 1$). The opposite limit, large wavelength or small D^* , corresponds to data confined to a thin sheet or slice taken out of three-dimensional space. In this limit, we have $\tilde{F}(k_z) \approx \tilde{F}(0) = \int dz F(z)$, and

$$P_p(q) \rightarrow \int \frac{dk_z}{2\pi} P[(q^2 + k_z^2)^{1/2}] \quad (23)$$

$$B_p(\mathbf{q}_1, \mathbf{q}_2, \mathbf{q}_3) \rightarrow \int \frac{dk_{z1}}{2\pi} \frac{dk_{z2}}{2\pi} B(\mathbf{q}_1, k_{z1}; \mathbf{q}_2, k_{z2}; \mathbf{q}_3, k_{z3}) \quad (24)$$

($qD^* \rightarrow 0$), where $k_{z3} = -(k_{z1} + k_{z2})$.

3. Numerical Results

In this section we presents results of numerical integrations of equations (18,19). For numerical calculations we take $F(z) = (z/D^*)e^{-z/D^*}$, $\tilde{F}(k_z) = 1/(1 - ik_z D^*)^2$. This analytically convenient form mimics the relative lack of nearby galaxies because of geometry and the rapid fall of the luminosity function above L^* . Because integration is a smoothing operation, we expect the general nature of the results to be insensitive to the precise behavior of F . For this F , integrals appearing above can be done analytically,

$$I_n = \int dz F^n(z) = n! (D^*/n)^{n+1}, \quad (25)$$

and so from equation (22) we have for large qD^*

$$\frac{Q_p}{Q} = \frac{I_1 I_3}{I_2^2} = \frac{32}{27}. \quad (26)$$

For our numerical study we use the perturbation theory form for the shape dependence of B ,

$$B(\mathbf{k}_1, \mathbf{k}_2, \mathbf{k}_3) = Q(\mathbf{k}_1, \mathbf{k}_2)P(k_1)P(k_2) + Q(\mathbf{k}_1, \mathbf{k}_3)P(k_1)P(k_3) + Q(\mathbf{k}_2, \mathbf{k}_3)P(k_2)P(k_3) \quad (27)$$

where

$$Q(\mathbf{k}_i, \mathbf{k}_j) = \frac{10}{7} + (\hat{\mathbf{k}}_i \cdot \hat{\mathbf{k}}_j) \left(\frac{k_i}{k_j} + \frac{k_j}{k_i} \right) + \frac{4}{7} (\hat{\mathbf{k}}_i \cdot \hat{\mathbf{k}}_j)^2 \quad (28)$$

(Fry 1984).

Figure 1 shows the projected $P_p(q)$ (eq. [18]) for $n = +1, 0, -1$, and -2 , evaluated for $D^* = 1$. Results scale with $D^* \neq 1$ as $P_p(q; D^*) = D^{*-n+1} P_p(qD^*)$. Dashed lines show the large- q result (eq. [20]), $P_p \sim q^n$. There is a change of characteristic behavior near $q = 1$. The behavior at small q , corresponding to scales much larger than the depth of the projection, is that of data on a thin two-dimensional plane sheet or slice embedded in three dimensions.

Figure 2 shows the dependence of the projected three-point amplitude $Q_p(\theta)$ on configuration shape for triangles with sides $q_1 = q$, $q_2 = q/2$, separated by angle θ . Curves are shown for $qD^* = 0.001, 0.01, 0.1, 1, 10, 100$, and 1000 , as indicated in the caption. The four windows show results for power spectrum indices $n = +1, 0, -1$, and -2 . In some cases, the curves for small qD^* overlap and are indistinguishable, as is also always the case for large qD^* . In the large- qD^* limit the projected result is the result in space multiplied by an overall factor, here $32/27$.

Projection changes the shape of of Q , making the curves in Figure 2 flatter at shallow depth, or at large wavelength, just as would a bias with $b > 1$. Misconstruing the flattening as an effect of bias gives the parameters $b = b_1$ and b_2/b^2 listed in Table 1. The rms difference between the projected Q and the fit Q , $\Delta^2 = \int d\theta (Q_p - Q_b)^2 / \pi$, is small, at most 0.0036, for $n = -2$ and $qD^* = 1$ and often much smaller. The difference between the fit value of b and 1 is of order $1/qD^*$ when qD^* is large.

4. Angular Projection

4.1. Full Sky Coverage

Typically, observations without distance information give galaxy positions not in Cartesian coordinates but in angle on the the sky; so we next consider the effects of projection onto the sphere. In spherical

coordinates, a position in space is specified by distance r from the origin and angular coordinates θ, ϕ , also denoted variously by solid angle Ω and unit vector $\hat{\mathbf{n}}$. Summed over r , the projected angular density on the sphere is

$$\mathcal{N}(\theta, \phi) = \int r^2 dr F(r) n(r, \theta, \phi), \quad (29)$$

with average value $\bar{\mathcal{N}} = \bar{n} \int r^2 dr F(r)$.

The natural transform on the sky is by spherical harmonics. For comparison with later results, we compute first the full spherical harmonic transform. First, we compute the amplitude

$$\tilde{\mathcal{N}}_{\ell m} = \int d\Omega \mathcal{N}(\Omega) Y_{\ell m}^*. \quad (30)$$

We wish to relate moments of this amplitude to the spatial power spectrum. The first step is to express $\tilde{\mathcal{N}}_{\ell m}$ in terms of the Fourier amplitude $\tilde{n}(\mathbf{k})$ defined in equation (12). Useful relations towards this end include the expansion of a plane wave in spherical coordinates,

$$e^{ikz} = \sum_{\ell} i^{\ell} (2\ell + 1) j_{\ell}(kr) P_{\ell}(\cos \theta) \quad (31)$$

and the addition theorem for spherical harmonics,

$$4\pi \sum_m Y_{\ell m}(\hat{\mathbf{n}}_1) Y_{\ell m}^*(\hat{\mathbf{n}}_2) = (2\ell + 1) P_{\ell}(\hat{\mathbf{n}}_1 \cdot \hat{\mathbf{n}}_2), \quad (32)$$

where P_{ℓ} is the Legendre polynomial of order ℓ (Jackson 1975). From these, we obtain the transform amplitude

$$\tilde{\mathcal{N}}_{\ell m} = \int \frac{d^3 k}{(2\pi)^3} \tilde{n}(\mathbf{k}) \tilde{F}_{\ell}(k) 4\pi i^{\ell} Y_{\ell m}^*(\hat{\mathbf{k}}), \quad (33)$$

where $\tilde{F}_{\ell}(k) = \int r^2 dr F(r) j_{\ell}(kr)$ is real.

Only $\tilde{\mathcal{N}}_{00}$ has a nonvanishing expectation, $\langle \tilde{\mathcal{N}}_{00} \rangle = \sqrt{4\pi} \bar{n} \tilde{F}_0(0)$. The second moment $\langle \tilde{\mathcal{N}}_{\ell_1 m_1} \tilde{\mathcal{N}}_{\ell_2 m_2} \rangle$ vanishes unless $\ell_1 = \ell_2, m_1 = -m_2$. Normalized by $\langle \tilde{\mathcal{N}}_{00} \rangle$ we have

$$\mathcal{P}_{\ell} = \frac{\langle |\tilde{\mathcal{N}}_{\ell, m}|^2 \rangle}{\langle \tilde{\mathcal{N}}_{00} \rangle^2} = \int \frac{d^3 k}{(2\pi)^3} \frac{\tilde{F}_{\ell}^2(k)}{\tilde{F}_0^2(0)} P(k), \quad (34)$$

independent of m .

When ℓ is large, the sequence of functions $\tilde{F}_{\ell}(k)$ approaches a scaling function, $\tilde{F}_{\ell}(k) \sim \ell^{3/2} \tilde{F}_s(kD^*/\ell)$, where $\tilde{F}_s(y)$ is peaked around $y \sim 1$ and has width $\Delta y \sim 1$, as shown in Figure 4. With a rapidly decreasing $F(r)$, this can be understood as the main contribution to $\tilde{F}_{\ell}(k)$ arising from the first peak of $j_{\ell}(x)$, which appears at $kD^* \approx \ell$. With guidance from the small angle limit below, we find $\tilde{F}_s = (\pi/2)^{1/2} y^{-3} e^{-1/y}$, which agrees with the solid line so well as to be indistinguishable in the figure. Thus, for large ℓ we have the asymptotic expression

$$\mathcal{P}_{\ell} \rightarrow P_s(\ell) = \int \frac{d^3 y}{(2\pi)^3} \frac{\tilde{F}_s^2(y)}{\tilde{F}_0^2(0)} P(\ell y/D^*). \quad (35)$$

For power law $P(k) \sim k^n$, equation (35) gives $P_s(\ell) \sim P(\ell/D^*) \sim (\ell/D^*)^n$. Results for \mathcal{P}_{ℓ} for power law $P(k)$ are plotted in Figure 3; the scaling result $P_s(\ell)$ is plotted as dashed lines. The behavior is similar to that seen in Figure 1, approaching the scaling result for large ℓ .

The third moment of the amplitude in equation (33) is

$$\begin{aligned} \langle \tilde{\mathcal{N}}_{\ell_1 m_1} \tilde{\mathcal{N}}_{\ell_2 m_2} \tilde{\mathcal{N}}_{\ell_3 m_3} \rangle &= \int \frac{d^3 k_1}{(2\pi)^3} \frac{d^3 k_2}{(2\pi)^3} \frac{d^3 k_3}{(2\pi)^3} \tilde{F}_{\ell_1}(k_1) \tilde{F}_{\ell_2}(k_2) \tilde{F}_{\ell_3}(k_3) (4\pi\bar{n})^3 i^{\ell_1 + \ell_2 + \ell_3} \\ &\quad \times [(2\pi)^3 \delta_D(\mathbf{k}_1 + \mathbf{k}_2 + \mathbf{k}_3)] B_{123} Y_{\ell_1 m_1}^*(\hat{\mathbf{k}}_1) Y_{\ell_2 m_2}^*(\hat{\mathbf{k}}_2) Y_{\ell_3 m_3}^*(\hat{\mathbf{k}}_3). \end{aligned} \quad (36)$$

Indices ℓ_1 , ℓ_2 , and ℓ_3 specify the overall frequency of angular oscillation of $Y_{\ell m}$, while m_1 , m_2 , and m_3 specify the orientation of the oscillation with respect to a chosen polar axis. Because the universe is believed to be statistically isotropic, we are interested in the part of this expression that is invariant under rotations. This can be expressed using properties of the Wigner 3- j coefficients (see Edmonds 1957), related to Clebsch-Gordan coefficients by

$$\begin{pmatrix} j_1 & j_2 & j_3 \\ m_1 & m_2 & m_3 \end{pmatrix} = \frac{(-1)^{j_1 - j_2 + m_3}}{(2j_3 + 1)^{1/2}} \langle j_1 m_1 j_2 m_2 | j_3 - m_3 \rangle. \quad (37)$$

Under a rotation $D(\omega)$ with Euler angles $\omega = (\alpha, \beta, \gamma)$, states with the same j but different values of m mix,

$$D(\omega) | j m \rangle = \sum_{m'} \mathcal{D}_{mm'}^{(j)} | j m' \rangle \quad (38)$$

where the \mathcal{D} are matrix elements of $D(\omega)$,

$$\mathcal{D}_{mm'}^{(j)} = \langle j m' | D(\omega) | j m \rangle, \quad (39)$$

with

$$\mathcal{D}_{m0}^{(\ell)}(\omega) = (-1)^m \left(\frac{4\pi}{2\ell + 1} \right)^{1/2} Y_{\ell m}(\beta, \alpha). \quad (40)$$

In terms of the rotation matrix elements, the effect of a rotation on the 3- j coefficient is

$$\sum_{m'_1, m'_2, m'_3} \mathcal{D}_{m'_1 m_1}^{(j_1)} \mathcal{D}_{m'_2 m_2}^{(j_2)} \mathcal{D}_{m'_3 m_3}^{(j_3)} \begin{pmatrix} j_1 & j_2 & j_3 \\ m'_1 & m'_2 & m'_3 \end{pmatrix} = \begin{pmatrix} j_1 & j_2 & j_3 \\ m_1 & m_2 & m_3 \end{pmatrix}; \quad (41)$$

if we take $m_1 = m_2 = m_3 = 0$, we then have

$$\sum_{m_1, m_2, m_3} \begin{pmatrix} \ell_1 & \ell_2 & \ell_3 \\ m_1 & m_2 & m_3 \end{pmatrix} Y_{\ell_1 m_1} Y_{\ell_2 m_2} Y_{\ell_3 m_3} = \left[\frac{(2\ell_1 + 1)(2\ell_2 + 1)(2\ell_3 + 1)}{(4\pi)^3} \right]^{1/2} \begin{pmatrix} \ell_1 & \ell_2 & \ell_3 \\ 0 & 0 & 0 \end{pmatrix}. \quad (42)$$

Nonvanishing contributions to the sum have $m_1 + m_2 + m_3 = 0$; the ℓ_i must also obey triangle inequalities, $|\ell_1 - \ell_2| \leq \ell_3 \leq \ell_1 + \ell_2$, etc.; and the sum $\ell_1 + \ell_2 + \ell_3$ must also be even. Removing the dependence on m leaves a result independent of orientation of the polar axis. This leads us to consider the averaged angular bispectrum,

$$\begin{aligned} \mathcal{B}_{\ell_1 \ell_2 \ell_3} &= \sum_{m_1, m_2, m_3} \begin{pmatrix} \ell_1 & \ell_2 & \ell_3 \\ m_1 & m_2 & m_3 \end{pmatrix} \frac{\langle \tilde{\mathcal{N}}_{\ell_1 m_1} \tilde{\mathcal{N}}_{\ell_2 m_2} \tilde{\mathcal{N}}_{\ell_3 m_3} \rangle}{\langle \tilde{\mathcal{N}}_{00} \rangle^3} \\ &= I_{\ell_1 \ell_2 \ell_3} \int \frac{d^3 k_1}{(2\pi)^3} \frac{d^3 k_2}{(2\pi)^3} \frac{d^3 k_3}{(2\pi)^3} \frac{\tilde{F}_{\ell_1}(k_1)}{\tilde{F}_0(0)} \frac{\tilde{F}_{\ell_2}(k_2)}{\tilde{F}_0(0)} \frac{\tilde{F}_{\ell_3}(k_3)}{\tilde{F}_0(0)} B(\mathbf{k}_1, \mathbf{k}_2, \mathbf{k}_3), \end{aligned} \quad (43)$$

where $\mathbf{k}_3 = -\mathbf{k}_1 - \mathbf{k}_2$ and the coefficient $I_{\ell_1 \ell_2 \ell_3}$ is

$$I_{\ell_1 \ell_2 \ell_3} = [(2\ell_1 + 1)(2\ell_2 + 1)(2\ell_3 + 1)]^{1/2} \begin{pmatrix} \ell_1 & \ell_2 & \ell_3 \\ 0 & 0 & 0 \end{pmatrix}. \quad (44)$$

This angular averaging was introduced by Spergel & Goldberg (1998) for the microwave background. This is formally very similar to the Cartesian result, equation (19). For the behavior at large ℓ we look at partial sky coverage in the small angle approximation in the next section.

4.2. Partial Sky Coverage

In practice, there is no galaxy or cluster catalog with complete sky coverage, and in deep catalogs interesting scales cover only small angles. It is far more efficient computationally to treat a small square patch of sky as flat and use a Fourier transform, or especially FFT, rather than the spherical harmonic transform (Fry & Seldner 1982). Our final goal is to determine just what the result is of such a procedure.

The Fourier transform in “flat” angular coordinates $\boldsymbol{\theta}$ is

$$\tilde{n}_p(\boldsymbol{\kappa}) = \int_{\Lambda} d^2\theta n_p(\boldsymbol{\theta}) e^{-i\boldsymbol{\kappa}\cdot\boldsymbol{\theta}}. \quad (45)$$

where $\boldsymbol{\theta} = (\theta_1, \theta_2) = (\theta \cos \phi, \theta \sin \phi)$ runs over a small patch of sky, say a square of side Λ , and $\boldsymbol{\kappa}$ is a Fourier frequency conjugate to $\boldsymbol{\theta}$. The projected amplitude $\tilde{n}_p(\boldsymbol{\kappa})$ in terms of $\tilde{n}(\mathbf{k})$ is then in full

$$\tilde{n}_p(\boldsymbol{\kappa}) = \int_{\Lambda} d^2\theta e^{-i\boldsymbol{\kappa}\cdot\boldsymbol{\theta}} \int \frac{d^3k}{(2\pi)^3} \tilde{F}_\ell(k) \tilde{n}(\mathbf{k}) \sum_{\ell,m} 4\pi i^\ell Y_{\ell m}(\hat{\mathbf{n}}) Y_{\ell m}^*(\hat{\mathbf{k}}), \quad (46)$$

For the full sky transform, the integrals over angles involved orthogonal functions, leading to the simple result in equation (33). The projected second moment of \tilde{n}_p here is

$$\langle \tilde{n}_p(\boldsymbol{\kappa}_1) \tilde{n}_p(\boldsymbol{\kappa}_2) \rangle = \bar{n}_p^2 \sum_{\ell=0}^{\infty} \Delta_\ell(\boldsymbol{\kappa}_1, \boldsymbol{\kappa}_2) \mathcal{P}_\ell \quad (47)$$

where \mathcal{P}_ℓ is as in equation (34) and

$$\Delta_\ell(\boldsymbol{\kappa}_1, \boldsymbol{\kappa}_2) = (2\ell+1) \int_{\Lambda} d^2\theta_1 d^2\theta_2 e^{-i\boldsymbol{\kappa}_1\cdot\boldsymbol{\theta}_1} e^{-i\boldsymbol{\kappa}_2\cdot\boldsymbol{\theta}_2} P_\ell(\hat{\mathbf{n}}_1 \cdot \hat{\mathbf{n}}_2). \quad (48)$$

This integral behaves as an effective δ -function, peaked for $\boldsymbol{\kappa}_1 + \boldsymbol{\kappa}_2 = 0$ and at $\ell = |\kappa|$, but smeared in κ and ℓ over roughly $\pm(2\pi/\Lambda)$, or ± 1 wave per box. This is shown in Figure 5 for $\boldsymbol{\kappa} = (8, 0)$, $(7, 4)$, and $(5, 6)$, in units of $2\pi/\Lambda = 18.947$, each with approximately the same magnitude, $\kappa = 8, 8.062$, and 7.810 , respectively, but different orientations. Both the location and width of the peaks behave as expected.

Useful expressions can be obtained when Λ is small, so that $\mathbf{r} = (r\theta \cos \phi, r\theta \sin \phi, r)$. Integrals over angles such as

$$\int_{-\Lambda/2}^{+\Lambda/2} d\theta_x e^{i(k_x r - \kappa_x)} = \frac{\sin[\Lambda(k_x r - \kappa_x)/2]}{(k_x r - \kappa_x)/2} \quad (49)$$

are effectively δ -functions, with resolution in κ of $\pm 2\pi/\Lambda$. With this, the projected amplitude becomes

$$\tilde{n}_p(\boldsymbol{\kappa}) = \int \frac{dk}{2\pi} \int dr F(r) e^{ikr} \tilde{n}(\boldsymbol{\kappa}/r, k) = \int \frac{d\lambda}{2\pi} \int \frac{du}{u^2} F(1/u) e^{i\kappa\lambda} \tilde{n}(\boldsymbol{\kappa}u, \kappa u \lambda), \quad (50)$$

where $r = 1/u$ and $k = \lambda \kappa u$. Then we have for the second moment

$$\langle \tilde{n}_p(\boldsymbol{\kappa}_1) \tilde{n}_p^*(\boldsymbol{\kappa}_2) \rangle = \bar{n}^2 (2\pi)^2 \delta_D(\phi_1 - \phi_2) \frac{1}{\kappa_2} \int \frac{d\lambda}{2\pi} e^{i\lambda \Delta \kappa} \int \frac{du_1}{u_1^2 u_2^2} F(1/u_1) F(1/u_2) P[\kappa_1 u_1 (1 + \lambda^2)^{1/2}], \quad (51)$$

where the δ -function in the second moment of $\tilde{n}(\mathbf{k})$ require that $\boldsymbol{\kappa}_1$ and $\boldsymbol{\kappa}_2$ are in opposite directions and thus $u_2 \kappa_2 = u_1 \kappa_1$. For power law $P(k) \sim k^n$ the power spectrum factors to $(1 + \lambda^2)^{n/2} P(\kappa_1 u_1)$. The integral

over λ can be expressed in terms of modified Bessel functions of order $\pm(n+1)/2$ for non-integer n , while for negative integer n ,

$$\int \frac{d\lambda}{2\pi} e^{i\lambda\Delta\kappa} (1+\lambda^2)^{n/2} = \begin{cases} \delta_D(\Delta\kappa) & n=0, \\ \frac{1}{\pi} K_0(|\Delta\kappa|) & n=-1, \\ \frac{1}{2} e^{-|\Delta\kappa|} & n=-2, \\ \frac{1}{\pi} |\Delta\kappa| K_1(|\Delta\kappa|) & n=-3. \end{cases} \quad (52)$$

All of these are appreciable only for $|\Delta\kappa| \lesssim 1$, fall off exponentially for large $\Delta\kappa$, and integrate to 1; so for any n the integral is once again effectively a δ -function of $\Delta\kappa$, to an accuracy ± 1 , where for small Λ , κ is large. Requiring $\kappa_2 = \kappa_1$ implies $u_2 = u_1$ also, and thus the second moment of the projected Fourier amplitude in equation (51) becomes

$$\langle \tilde{n}_p(\kappa_1) \tilde{n}_p(\kappa_2) \rangle = \bar{n}_p^2 [(2\pi)^2 \delta_D(\kappa_1 + \kappa_2)] P_p(\kappa), \quad (53)$$

where

$$P_p(\kappa) = \frac{1}{[\int F(1/u) du/u^4]^2} \int \frac{du}{u^4} F^2(1/u) P(\kappa u). \quad (54)$$

Although this expression was obtained for a power law $P(k)$, to the extent that the integral over λ in equation (52) is effectively a δ -function, this ought to apply for any well-behaved power spectrum. This equation is the same Kaiser's (1992) equation (A.2), obtained here by a different path, and is equivalent to the scaling result in equation (35) for $P_s(\ell)$ at large ℓ . For $F(r) = \exp(-r/D^*)$, this gives us the form of the scaling function, $\tilde{F}_s(y) = (\pi/2)^{1/2} y^{-3} e^{-1/y}$.

For the third moment, we have

$$\begin{aligned} \langle \tilde{n}_p(\kappa_1) \tilde{n}_p(\kappa_2) \tilde{n}_p(\kappa_3) \rangle &= \bar{n}^3 \int \frac{dk_1}{2\pi} \frac{dk_2}{2\pi} \frac{dk_3}{2\pi} \int \frac{du_1}{u_1^2} \frac{du_2}{u_2^2} \frac{du_3}{u_3^2} F(1/u_1) F(1/u_2) F(1/u_3) \\ &\quad \times [(2\pi)^3 \delta_D(\kappa_1 + \kappa_2 + \kappa_3)] B(u\kappa_1, k_1; u\kappa_2, k_2; u\kappa_3, k_3), \end{aligned} \quad (55)$$

where as before $u = 1/r$. One component of the momentum-conserving δ -function constrains $k_1 + k_2 + k_3 = 0$; the two others $\sum u_i \kappa_i = 0$. One of these last, in any direction not perpendicular to κ_1 , can be taken to give the value of u_1 , and the second component to give u_2 , in terms of u_3 and the κ_i , leaving

$$\begin{aligned} \langle \tilde{n}_p(\kappa_1) \tilde{n}_p(\kappa_2) \tilde{n}_p(\kappa_3) \rangle &= \bar{n}^3 \int \frac{dk_1}{2\pi} e^{ik_1 \Delta\kappa_{13}} \int \frac{dk_3}{2\pi} e^{ik_3 \Delta\kappa_{23}} \int \frac{du_1}{u_1^2 u_2^2 u_3^2} \\ &\quad \times F(1/u_1) F(1/u_2) F(1/u_3) B(u_1 \kappa_1, u_2 \kappa_2, u_3 \kappa_3) \end{aligned} \quad (56)$$

As was found for the second moment, the k -integrals are effectively δ -functions, enforcing constraints that require the triangle in the κ_i to be closed; when these are satisfied all three u_i are equal. Thus, we have finally

$$\langle \tilde{n}_p(\kappa_1) \tilde{n}_p(\kappa_2) \tilde{n}_p(\kappa_3) \rangle = \bar{n}_p^3 [(2\pi)^2 \delta_D(\kappa_1 + \kappa_2 + \kappa_3)] B_p(\kappa_1, \kappa_2, \kappa_3), \quad (57)$$

$$B_p(\kappa_1, \kappa_2, \kappa_3) = \frac{1}{[\int du F(1/u) u^4]^3} \int \frac{du}{u^4} F^3(1/u) B(u\kappa_1, u\kappa_2, u\kappa_3). \quad (58)$$

This is what we have been aiming for, an expression for the projected bispectrum in terms of the full bispectrum in space and the selection function F . For power law $P(k) \sim k^n$, $B(u\kappa_i) = u^{2n} B(\kappa_i)$, and so the projected bispectrum has the same shape dependence as the bispectrum in space, with an overall multiplicative factor

$$Q_p = \frac{[\int du F^3(1/u) u^{2n-4}] [\int du F(1/u) u^{-4}]}{[\int du F^2(1/u) u^{n-4}]^2} Q_{123}. \quad (59)$$

Written in terms of $r = 1/u$, this is the same projection factor obtained by Groth & Peebles (1977) for Q in space and by Bernardeau (1995) and Gaztañaga & Bernardeau (1998) for the skewness S_3 .

As is apparent in equations (54) and (58), at fixed angles we are probing clustering on physical scales $\Delta r = r\Delta\theta$; and as r ranges over a broad selection function this can be a substantial variation. For a power spectrum that is not a simple power law, the effect of projection depends on how much the effective index $n_{\text{eff}} = d \log P / d \log k$ varies over the extent of the selection function. An example is shown in Figures 6 and 7 for the cold dark matter (CDM) power spectrum, as parametrized by Bardeen et al. (1986), for $\Omega = 0.3$, $h = 0.7$. The CDM spectrum has $n = +1$ as $k \rightarrow 0$ and $n \rightarrow -3$ as $k \rightarrow \infty$, and the projected spectrum has these limits also. Where the effective index is almost constant, the projected power is the same as would be obtained for a power-law spectrum with the same n . However, for values of κ near the peak the effective index varies enough to give a visibly different result. For the bispectrum, the effects of projection include a change in the amplitude of the variation with angle, the effect of a linear bias parameter $b \neq 1$; or as an overall shift in value, similar to a quadratic bias parameter $b_2 \neq 0$; or a change in the dependence on configuration that is not well fit by a local bias. Over the range of scales of the Lick catalog (Fry 1994), which corresponds to $\kappa = 25\text{--}150$, the apparent bias parameters in Table 2 differ from 1 by about 10% to only 2% at the scales most heavily weighted.

5. Discussion

In this paper we have investigated the effects of projection on the power spectrum and bispectrum in a variety of geometries. In general, projection is a smoothing operation, smearing out the dependence of the power spectrum and bispectrum on scale and the dependence of the bispectrum on configuration shape.

The degree of smoothing depends on the depth of the projection. For projection along a Cartesian direction we observe a range of behavior as this depth varies from very shallow to very deep. On scales small compared to the depth or wavenumbers q such that qD^* is large, except for an overall numerical factor projection has minimal effect; but the result of smoothing becomes increasingly visible as q decreases, with a qualitative change in behavior at $qD^* \approx 1$. For power law $P(k) \sim k^n$, the projected power spectrum is also $P_p(q) \sim q^n$ with the same value of n for large qD^* but the slope becomes noticeably shallower for small qD^* . For the bispectrum we can quantify the result by the apparent bias factors given in Table 1. For large qD^* the apparent bias parameters differ from $b = 1$ and $b_2 = 0$ by an amount of order $1/qD^*$ or smaller. This can be traced to equations (18) and (19), where it can be seen that the range of scales contributing has spread $\Delta k/k \sim 1/qD^*$.

The projected full sky angular distribution has power \mathcal{P}_ℓ in spherical harmonic amplitudes as given in equation (34). For a power-law power spectrum, the scaling limit in equation (35) gives $\mathcal{P}_\ell \rightarrow P_s(\ell) \sim \ell^n$ with the same n , while the exact result at small ℓ departs from this scaling limit in a way similar to the behavior of Cartesian result as $qD^* \rightarrow 1$. Restricting the angular transform to a small portion of the sky of size Λ smears the result over values of ℓ over a range $\pm 2\pi/\Lambda$. Once again the limiting behavior for large κ , where κ is a transform variable conjugate to θ , is $P_p(\kappa) \sim \kappa^n$.

Additional effects enter when the power spectrum is not a pure power law, The integrals in equation (54) and equation (58), and the obvious generalization for the n -point spectrum

$$B_{n,p}(\kappa_1, \dots, \kappa_n) = \frac{1}{[\int du F(1/u)/u^4]^n} \int \frac{du}{u^4} F^n(1/u) B_n(u\kappa_1, \dots, u\kappa_n) \quad (60)$$

$(\sum \kappa_i = 0)$, average the spatial function over the range of scales covered by the selection function $F(r)$. When the effective index $n_{\text{eff}} = d \log P / d \log k$ has little dependence on scale, the power-law results still remain approximately valid, but when n_{eff} is changing appreciably over the scales sampled by F the projected functions can vary greatly, manifesting as apparent values b and b_2 .

From what we have learned above, to avoid introducing artifacts of projection in analyses of data we should limit consideration to scales where $\kappa \gg 1$, and for angular transform on a domain of side Λ to $\kappa\Lambda > 1$ as well. These restrictions appear to be satisfied in the Lick analysis (Fry 1994), for which $\kappa = 25\text{--}152$ and $\kappa\Lambda = 31\text{--}188$. This would appear to suggest that the weak shape dependence of the Lick bispectrum (Fry & Seldner 1982; Fry 1994) cannot be entirely ascribed to projection (but could be from nonlinear evolution, Scoccimarro et al. 1998).

Planned future microwave background experiments will eventually lead to precise measurements of cosmological parameters such as the Hubble constant H_0 , the fraction of critical density Ω_0 , and the cosmological constant Λ , and also of properties of the primordial power spectrum such as spectral index n and normalization Q . On the scales of galaxy clustering, what we will then be studying will be details of the modulation of primordial power by the dark matter. In order to do that, we must be able to measure bias parameters. Study of the galaxy bispectrum appears to be one tool with the potential to do this, and projection does not appear to introduce unsurmountable difficulties.

A portion of this work was done while J.N.F. was a visitor at the Aspen Center for Physics. A similar subject has been addressed recently by Buchalter, Kamionkowski, & Jaffe (1999). Research supported in part by NASA grant NAG5-2835 at the University of Florida.

Table 1. Cartesian Projection Bias Parameters

n	qD^*	$1/b$	b_2/b^2	Δ_{rms}
+1	0.01	−0.0015	0.3598	8.65×10^{-6}
	0.1	−0.0668	0.4159	4.18×10^{-4}
	1	0.2911	0.4363	5.37×10^{-4}
	10	0.9858	0.0128	1.14×10^{-4}
	100	0.9993	0.0004	1.23×10^{-5}
	1000	0.9997	0.0003	1.19×10^{-5}
0	0.01	−0.0023	1.1689	2.83×10^{-4}
	0.1	0.0031	1.0335	1.49×10^{-3}
	1	0.3605	0.4826	5.50×10^{-4}
	10	0.9493	0.0358	3.10×10^{-4}
	100	0.9984	0.0013	5.67×10^{-5}
	1000	0.9993	0.0009	5.56×10^{-5}
−1	0.01	0.0272	1.4424	9.04×10^{-4}
	0.1	0.0923	1.0868	1.48×10^{-3}
	1	0.4519	0.4341	2.28×10^{-3}
	10	0.9511	0.0361	8.49×10^{-4}
	100	0.9984	0.0017	1.49×10^{-4}
	1000	0.9993	0.0012	1.46×10^{-4}
−2	0.01	0.2097	0.9742	5.94×10^{-4}
	0.1	0.2521	0.8458	5.17×10^{-4}
	1	0.5250	0.3788	3.60×10^{-3}
	10	0.9510	0.0372	1.33×10^{-3}
	100	0.9984	0.0020	2.34×10^{-4}
	1000	0.9993	0.0016	2.29×10^{-4}

Table 2. Angular Projection Bias Parameters

κ	n_{eff}	$1/b$	b_2/b^2	Δ_{rms}
10	−0.543	1.081	0.183	1.34×10^{-2}
25	−1.289	1.019	0.167	8.17×10^{-3}
50	−1.733	0.993	0.109	3.84×10^{-3}
100	−2.026	0.981	0.068	1.37×10^{-3}
150	−2.152	0.978	0.054	6.62×10^{-4}
500	−2.405	0.977	0.029	3.53×10^{-4}
1000	−2.499	0.980	0.022	3.74×10^{-4}

REFERENCES

Bardeen, J. M., Bond, J. R., Kaiser, N., & Szalay, A. S. 1986, *ApJ*, 304, 15

Bernardeau, F. 1992, *ApJ*, 392, 1

Bernardeau, F. 1995, *A&A*, 301, 309

Bouchet, F. R., Juszkiewicz, R., Colombi, S. & Pellat, R. 1992, *ApJ*, 394, L5

Bouchet, F. R., Colombi, S., Hivon, E., & Juszkiewicz, R. 1995, *A&A*, 296, 575

Buchalter, A., Kamionkowski, M., & Jaffe, A. H. 1999, *astro-ph/9903486*

Edmonds, E. R. 1957, *Angular Momentum in Quantum Mechanics* (Princeton: Princeton Univ. Press).

Fry, J. N. 1984, *ApJ*, 279, 499

Fry, J. N. 1994, *Phys. Rev. Lett.*, 73, 215

Fry, J. N. & Gaztañaga, E. 1993, *ApJ*, 413, 447

Fry, J. N. & Seldner, M. 1982, *ApJ*, 259, 474

Gaztañaga, E., & Bernardeau, F. 1998, *A&A*, 331, 829

Goroff, M. H., Grinstein, B., Rey, S.-J., & Wise, M. 1986, *ApJ*, 311, 6

Groth, E. J. & Peebles, P. J. E. 1977, *ApJ*, 217, 385

Jackson, J. D. 1975, *Classical Electrodynamics*, Second ed. (New York: Wiley)

Jain, E., & Bertschinger, E. 1994, *ApJ*, 431, 495

Kaiser, N. 1992, *ApJ*, 388, 272

Limber, D. N. 1953, *ApJ*, 117, 134

Matarrese, S., Verde, L., & Heavens, A. F. 1997, *MNRAS*, 300, 747

Peebles, P. J. E. 1980, *The Large-Scale Structure of the Universe* (Princeton: Princeton Univ. Press)

Pollo, Agnieszka 1997, *Acta Astronomica*, 47, 413

Prudnikov, A. P., Brychkov, Yu. A., & Marichev, O. I. 1986, *Integrals and Series*, Vol. 2 (New York: Gordon & Breach)

Rubin, V. C. 1954, *Proc. N. A. S.*, 40, 541

Scoccimarro, R., Colombi, S., Fry, J. N., Frieman, J. A., Hivon, E., & Melott, A. L. 1998, *ApJ*, 496, 586

Scoccimarro, R., & Frieman, J. A. 1996a, *ApJS*, 105, 37

Scoccimarro, R., & Frieman, J. A. 1996b, *ApJ*, 473, 620

Spergel, D. N., & Goldberg, D. M. 1999, *astro-ph/9811252*

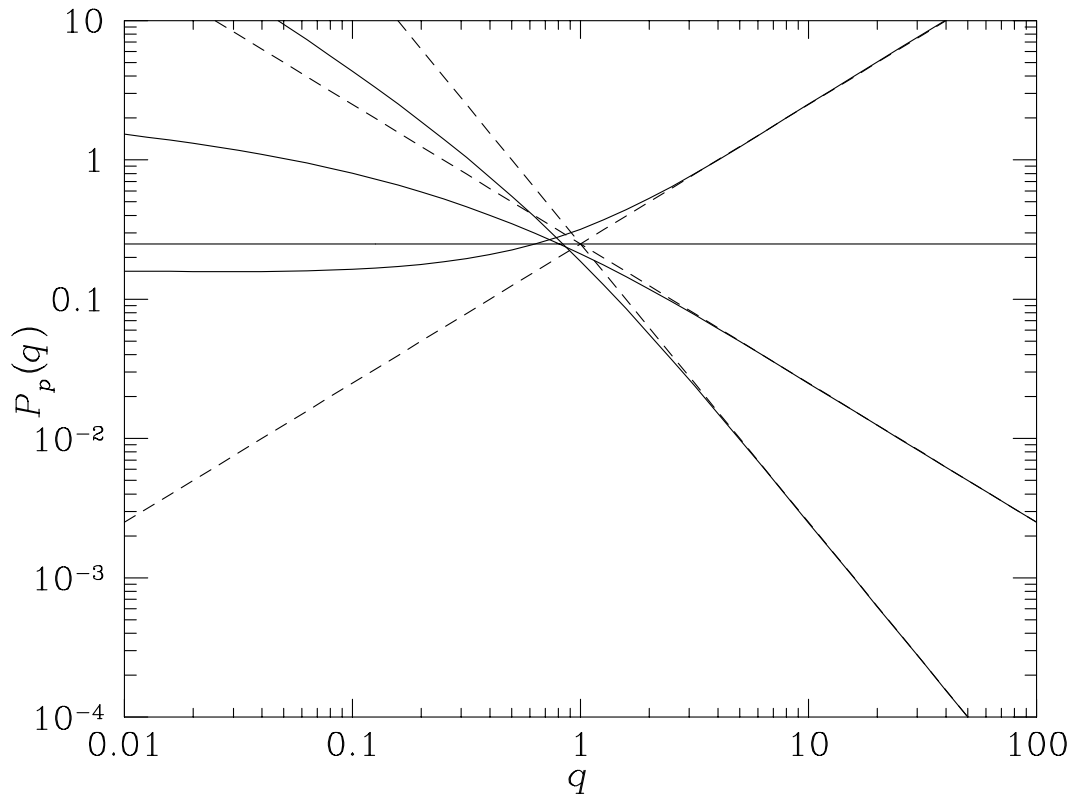


Fig. 1.— Projected $P_p(q)$ for $n = +1, 0, -1, -2$ evaluated for $D^* = 1$. Dashed lines show the large- q limit.

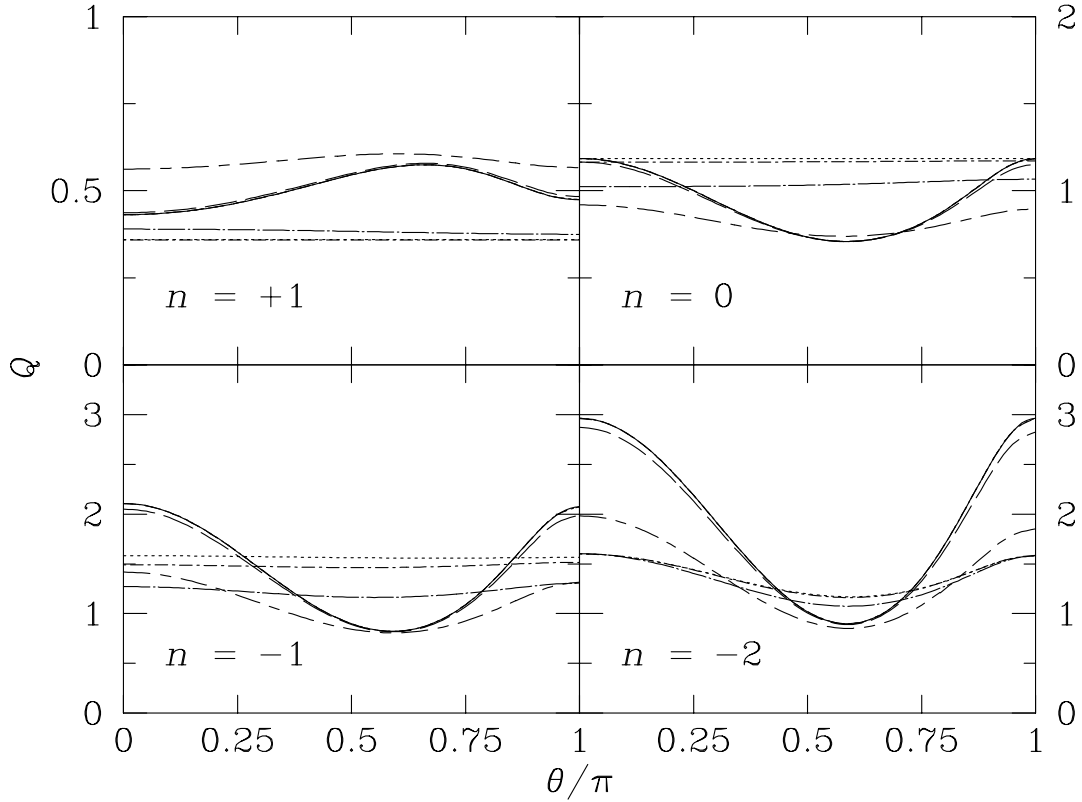


Fig. 2.— Projected $Q_p(\theta)$ for configurations with $q_1 = 1$, $q_2 = 1/2$, separated by θ , for power-law power spectra $P \sim k^n$ with $n = +1, 0, -1, -2$ as labelled. In each window, the solid curve shows the unprojected result scaled by the factor $32/27$; the dotted curve shows the projected result for $D^* = 0.001$; the dot-short dash curve $D^* = 0.01$; dot-long dash curve $D^* = 0.1$; short dash-long dash curve $D^* = 1$; long dashed curve $D^* = 10$. Results for $D^* = 100$ and $D^* = 1000$ are indistinguishable from solid curve.

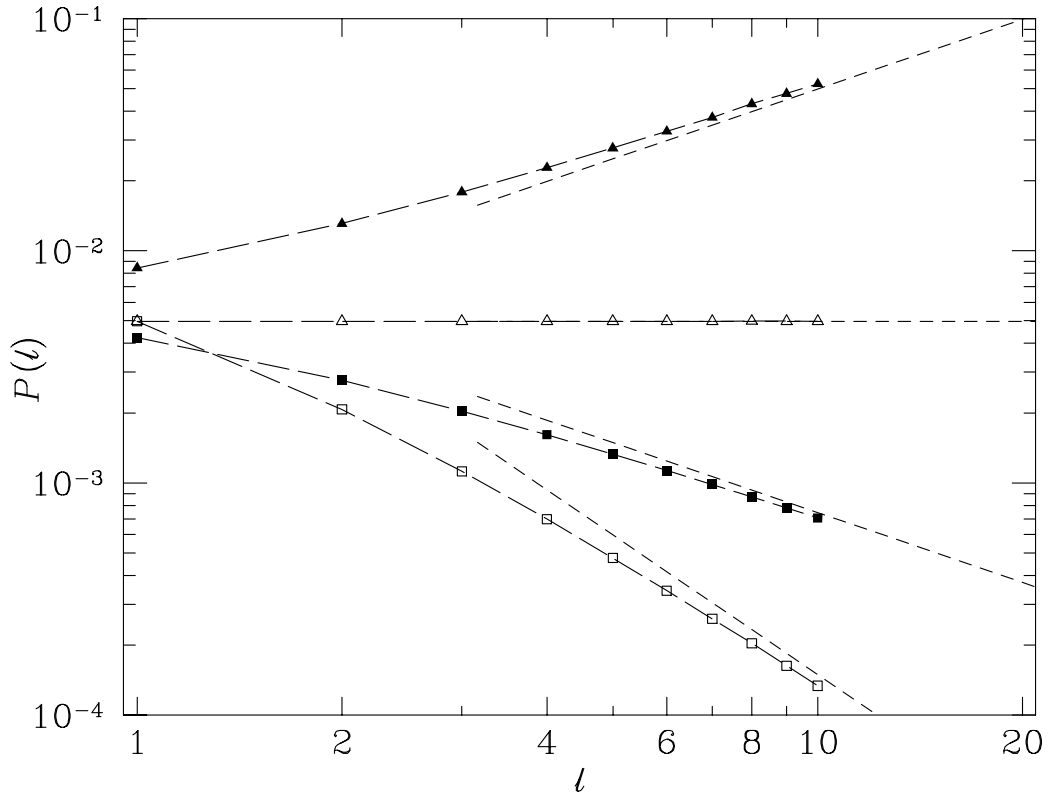


Fig. 3.— Projected angular power \mathcal{P}_ℓ vs. ℓ . Symbols show integrals over spherical Bessel functions for $\ell = 0$ through 10. Filled triangles denote $n = +1$, open triangles $n = 0$, filled squares $n = 0$, and open squares $n = -2$. Dashed lines show scaling result expected to hold for large ℓ .

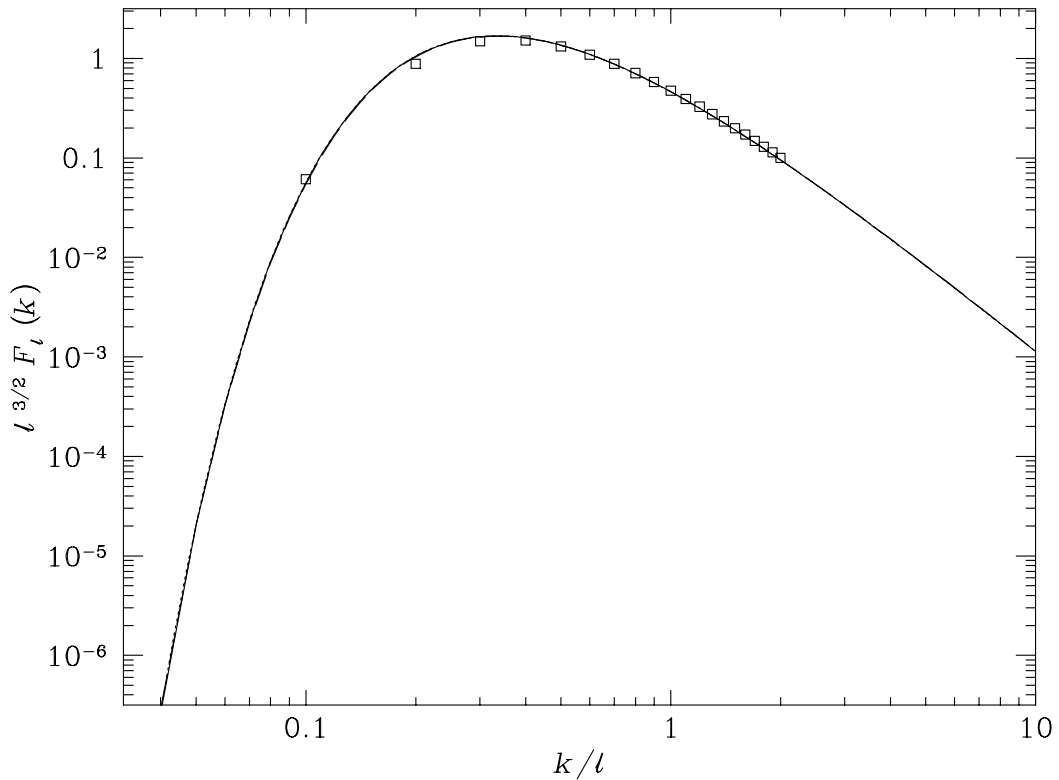


Fig. 4.— Scaled $\ell^{3/2} \tilde{F}_\ell$ vs. k/ℓ . Symbols show $\ell = 10$, dashed curve $\ell = 100$, solid curve $\ell = 1000$. The two curves are essentially indistinguishable.

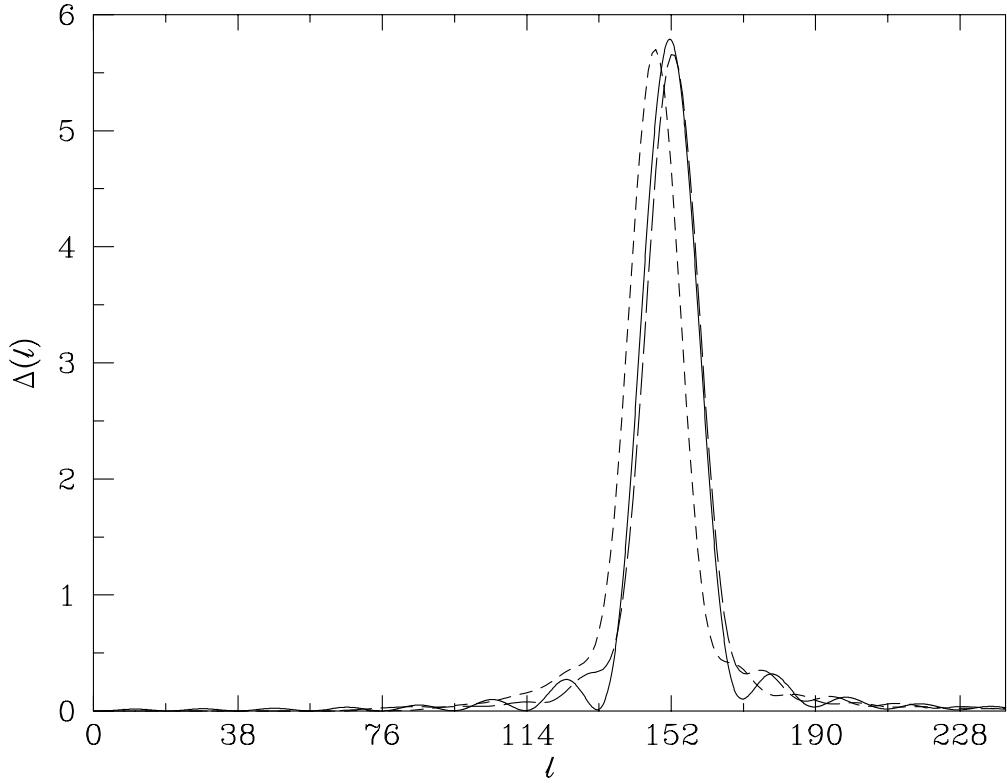


Fig. 5.— Integral $\Delta_\ell(\kappa_1, \kappa_2)$ (eq. [48]) plotted vs. ℓ . . Solid line shows $\kappa_1 = (8, 0)$ and $\kappa_2 = (-8, 0)$, long-dashed line shows $\kappa_1 = (7, 4)$ and $\kappa_2 = (-7, -4)$, and short-dashed line shows $\kappa_1 = (6, 5)$ and $\kappa_2 = (-6, -5)$, in units of $2\pi/\Lambda$ with $\Lambda = 19^\circ$.

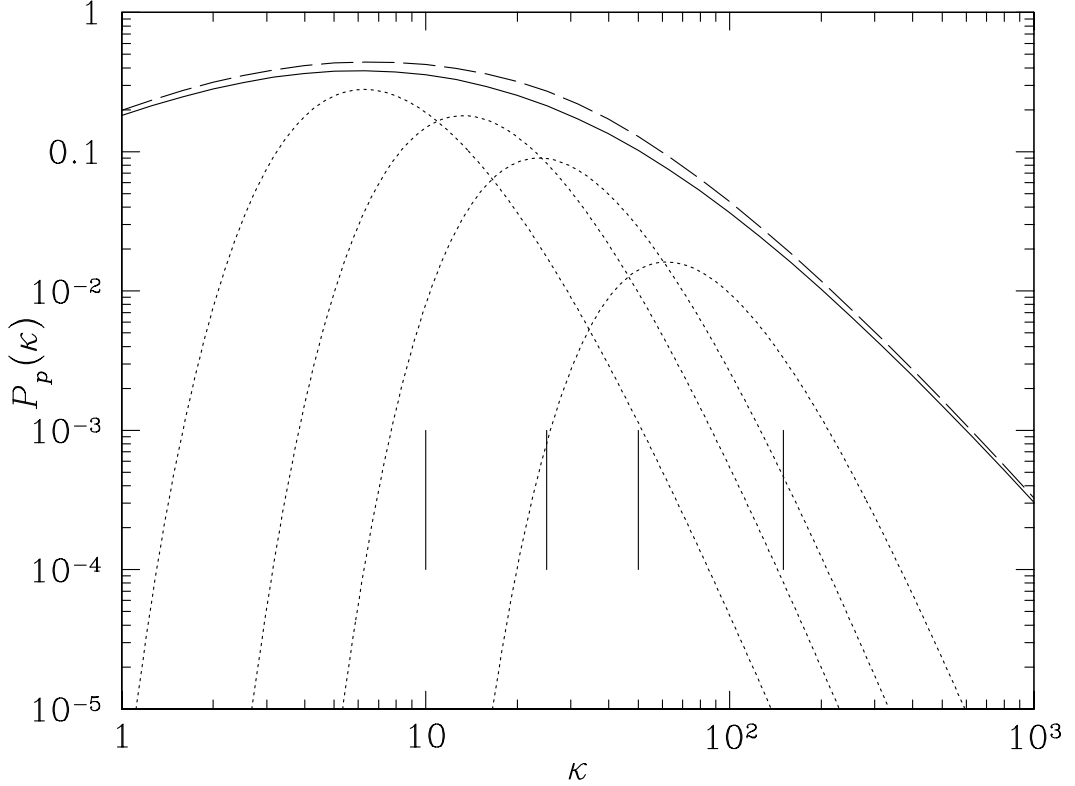


Fig. 6.— Projected $P_p(\kappa)$ obtained from equation (54) for the CDM power spectrum. The solid line shows the full integration of the CDM spectrum, while the long-dashed line shows what would be obtained for a power law spectrum with the effective local index n_{eff} . Vertical lines mark the values $\kappa = 10, 25, 50$, and 150 used in the next figure. The dotted lines show the spread of scales that contribute to the integrand, $\kappa^3 x^{-3} F^2(-\kappa/x) P(x/D^*)$ with $x = u/\kappa D^*$, for these four values of κ .

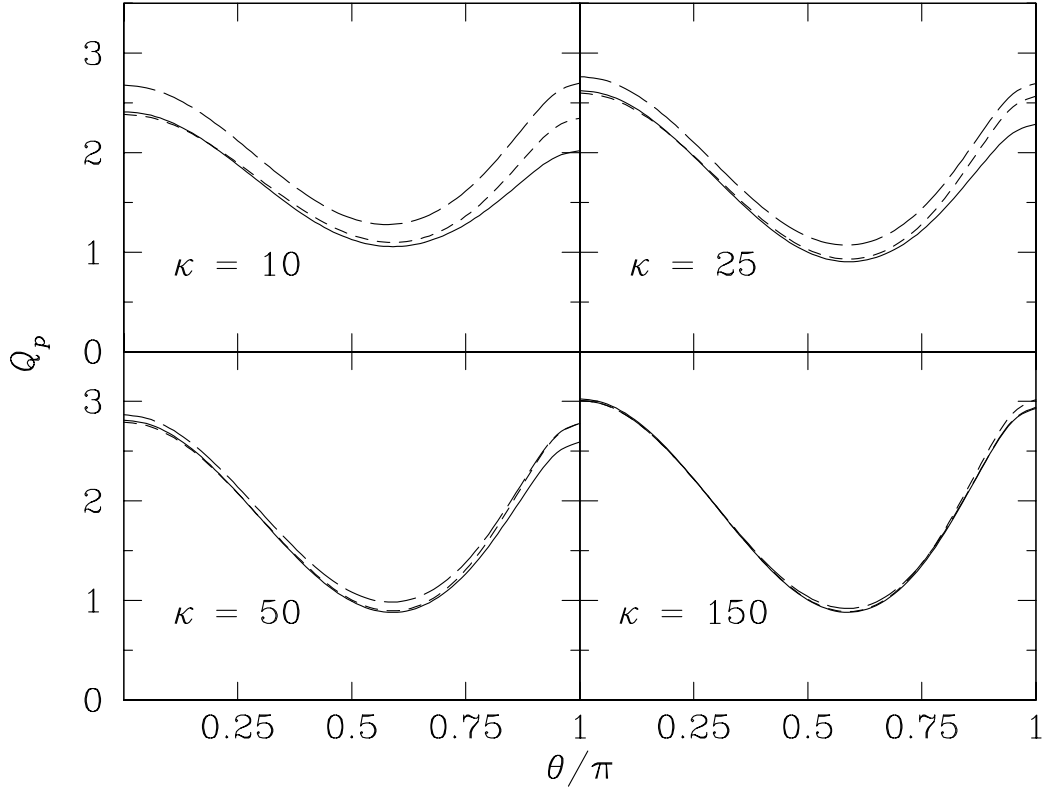


Fig. 7.— Projected $Q(\theta)$ obtained from equation (58) integrating over the CDM power spectrum for configurations with $\kappa_2 = \frac{1}{2}\kappa_1$ separated by angle θ for four values of $\kappa = \kappa_1$, as indicated. The long-dashed line shows the actual integrated projection, the short-dashed line shows projection of a power-law spectrum with index n_{eff} evaluated at κ_1 . The solid line shows Q before projection at scale $k = \kappa/D^*$, multiplied by the factor in equation (59).